Journal of Materials Science: Materials in Electronics (2018) 29:16824–16835
https://doi.org/10.1007/s10854-018-9777-6

Microstructural and optical properties of rare earth ions doped TiO_2 for potential white LED applications

Mohamed Zikriya[1] · Y. F. Nadaf[2] · C. Manjunath[3] · C. G. Renuka[1]

Received: 30 May 2018 / Accepted: 30 July 2018 / Published online: 2 August 2018

Abstract
Nano ceramics of pure TiO_2 and Dy^{3+}, Eu^{3+} and Tb^{3+} doped TiO_2 are prepared by hydrothermal method and these are characterized by using X-ray diffractometer (XRD), UV–Visible spectroscopy, field emission scanning electron microscopy (FESEM), high resolution transmission electron microscopy (HRTEM), and photoluminescence spectroscopy. XRD analysis revealed that the average particle size of the pure TiO_2 and Dy^{3+}, Eu^{3+} and Tb^{3+} doped TiO_2 are in the range of 45–35 nm and confirms the anatase phase. The FESEM and HRTEM analysis confirm that the obtained ceramics are in nano regime. The absorption spectrum revealed that the bandgap of the TiO_2 ceramics are in the range 3.14–3.2 eV. The PL analysis showed that the doping of Dy^{3+}, Eu^{3+} and Tb^{3+} had improved the luminescence behavior than the pure TiO_2 nanoparticles. Overall, by doping 0.5 mol% concentration of rare earth (RE) greatly alters the structural morphology and directly influence the luminescence behavior of TiO_2 and suitable for advanced optoelectronic applications. The color purity of the studied samples is found to be 91% for Dy^{3+}, 84% for Eu^{3+} and 73% for Tb^{3+} at the excitation of 345 nm, 376 nm and 350 nm respectively. The single-doped sample Eu^{3+}: TiO_2, Tb^{3+}: TiO_2 and Dy^{3+}: TiO_2 samples showed orange–red, blue–green and white emissions respectively.

1 Introduction

Titanium dioxide (TiO_2) nanoparticles have drawn interest due to their attractive solar cell, electronic, and photonic properties [1]. They have an extraordinary potential in different applications, for example, water purification, solar energy cell (DSSC), photocatalysis and gas-sensitive sensors [2, 3]. Doping with rare earths (REs) and transition metals are utilized to change and enhance the action of titania under visible light [4–8]. Doping of RE ion indicated exceptionally encouraging outcomes as for improvement of photograph reactivity of TiO_2. Recently, it was reported that by doping noble metals or transition metals in the TiO_2 matrix alter the surface absorption properties and improve the photocatalytic activity to a greater extend [9, 10]. Moreover, TiO_2 as a host material for doping metal ions have attracted lot of interest in order to achieve excellent luminescence behavior and photocatalytic activity [11]. Furthermore, by selective doping of RE ions into TiO_2 matrix, can slow down the recombination rate of electron–hole pair which leads to unique long lasting photo luminescent properties [12, 13]. Enhancing the luminescence behavior of RE doped semiconducting materials is a key factor influencing their practical applications.

Many RE ions like Eu^{3+}, Sm^{3+}, Er^{3+}, Tb^{3+} and Nd^{3+} [14] were doped into the TiO_2 to alters the emission in the UV to red region. Among other RE ions, the dysprosium ion (Dy^{3+}) doped materials cover fascinated to a great extent attention due to their white light emission by adjusting the yellow and blue emission [15]. Nevertheless, the emission is not completely controlled by the Dy^{3+} ions, the emission band may be altered base on the host crystal structure [16] because, the host lattice plays a significant role in altering the photo luminescence properties. In addition to that due to the large mismatch in the ionic radius between Dy^{3+} and Ti^{4+} and the charge imbalance, it is believed that the incorporation of Dy^{3+} ion into the lattices of TiO_2 is very difficult. From the literatures, it is clear that the luminescence property also depends on the preparation methodology [17]. RE doped

✉ C. G. Renuka
renubub@gmail.com

[1] Department of Physics, Bangalore University, Bengaluru, India

[2] Department of Physics and Research Center, Maharani's Science College for Women, Bengaluru, India

[3] Department of Physics, Sri Siddhartha Institute of Technology, Tumkur, India

materials can be synthesized using combustion method, pulsed laser deposition (PLD), chemical co-precipitation, forced hydrolysis and sol–gel method [18]. The hydrothermal method has been noticeable among all other methods; due to its capability to give materials of better morphology that is the main criteria in getting better enhanced emission. An incredible measure of research has been done to improve the hydrothermal method by hybridizing this technique with numerous different procedures. This effortless method does not require any catalyst, seed, unsafe and costly surfactant or layout along these lines it is potential for vast scale and ease generation with high superior quality of crystals [19]. Now in the present manuscript, we had modified suitably to justify the reason for selecting TiO_2 as host material for RE ion for luminescence applications. From the structural perspective, we require an adaptable and stable host which will maintain the supplanting of the inside cation with the coveted metal particles with no extensive changes in the host grid. Various studies have been recognized on the synthesis and optical characterization of Eu^{+3} doped TiO_2 with the objective of enhancing the luminescence of the Eu^{+3} ions by energy transfer from TiO_2. It has been conveyed that the semicrystalline, mesoporous TiO_2 films are perfect matrices for combining Eu^{+3} ions in which the sensitized photoluminescence [PL] emission is because of the energy transfer from the TiO_2 to Eu^{+3} ions in an TiO_2 region [20].

In the present research, we found that at low concentration dilution of RE ion can easily replace the host system and becomes a perfect energy transfer system. To the best of our knowledge, very few studied the effect of Dy^{3+} concentration in crystalline phase and Photo luminescence behavior of TiO_2. This preliminary research work on Dy^{3+} doped TiO_2 provides an opportunity to develop a suitable material for white light emitting diode, Eu^{3+} doped TiO_2 red light emitting and Tb^{3+} doped TiO_2 green light emitting. In this work, we synthesized pure, Dy^{3+}, Eu^{3+}, and Tb^{3+}doped TiO_2 nanoparticles using hydrothermal method without using any surfactant. Its complete micro-structural, optical and luminescence properties were studied.

2 Chemicals, preparation method and equipments

2.1 Chemicals and reagents

Dysprosium oxide (Dy_2O_3), Europium oxide oxide (Eu_2O_3), Terbium oxide (Tb_2O_7) Potassium persulphate ($K_2S_2O_8$), concentrated H_2SO_4, and Ammonia (NH_3) were all of spectroscopic grade with purity 99.9% purchased from Sigma Aldrich. Double distilled water was obtained from laboratory purification system. In the present study, Ilmenite extract were reduced to metatitanic acid using sulphate process. Metatitanic acid $[TiO(OH)_2]$ was used as a source material for the preparation of TiO_2. The complete procedure for the preparation of metatitanic acid is reported in M. Das et al. [21].

2.2 Sample preparation

The Pure and Dy^{3+}, Eu^{3+} and Tb^{3+}doped TiO_2 nanoparticles were synthesized through a hydrothermal method. Initially, 20 ml of metatitanic acid was added drop-wise in 8 ml of concentrated sulphuric acid (H_2SO_4) and heated till the solution became clear (say solution A). Secondly, 20 g of Potassium persulphate ($K_2S_2O_8$) powder taken in a beaker was heated to 400 °C for 1 h, to change solid to liquid state completely. Then 0.5 mol% concentration of Dy_2O_3, powder was mixed with $K_2S_2O_8$ solution and stirred well at constant temperature of 100 °C (say solution B). Now the solution B was added drop by drop into the solution A under vigorous stirring. Then meanwhile required quantity of concentrated H_2SO_4 was added drop by drop into the mixed solution to enhance the solubility to form a transparent solution. Moreover all the mixing has to be carrying out in the temperature range of 80–90 °C approximately to improve the solubility among solutions. Then the pH of the transparent solution was adjusted to 7 by adding Ammonia. Then the solution was aged for 12 h at room temperature, and then transfer the solution to 100 ml capacity autoclave Teflon lined stainless steel, by filling 3/4th of its quantity with reaction media (i.e. deionized water). The autoclave was heated at a temperature 160 °C for 12 h. The solution was then allowed to cool at room temperature the obtained residue is treated with deionized water and ethanol, dried the product at 40–50 °C temperature for 20 min to evaporate organic solvents and water. The white pure/RE doped TiO_2 nanocrystals are obtained as an end product was calcinated at 400 °C for 4 h. The same synthesis procedure is used to prepared Eu^{3+} and Tb^{3+}doped TiO_2.The flow chart of synthesis procedure of pure and RE doped TiO_2 is depicted in Fig. 1.

2.3 Equipments

The obtained samples are characterized by the different spectroscopic studies. To known the crystalline phase of the nanoparticles are analyzed with the aid of X-Ray Diffraction (XRD) using Rigaku diffractometer with Cu target K_α radiation (wavelength at 1.54 Å). The diffraction patterns were obtained with the angular range of $15° \leq 2\theta \leq 90°$ in a continuous mode with scanning speed of 2.0°/min. The surface morphology of the samples was examined by a field emission scanning electron microscopy (FESEM) TESCAN-MIRA 3 LMH, 2014 and transmission electron microscope (TEM) model JEOL JEM 2100 dual instrument with a discipline emission gun running at 200 kV. The absorption spectra of the synthesized samples have been studied by diffuse reflectance spectroscopy SIMADZU-UV-1800 in the range of 200–1100 nm. PL

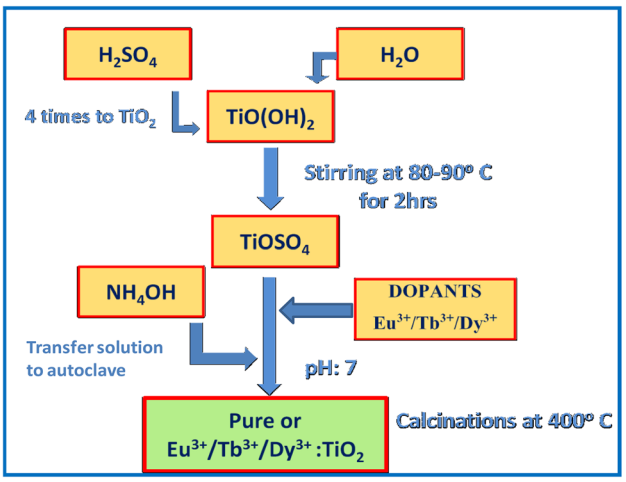

Fig. 1 Flow chart representation for the synthesis of pure and Eu^{3+}, Tb^{3+} and Dy^{3+}: TiO_2 (0.5 mol%) by hydrothermal method

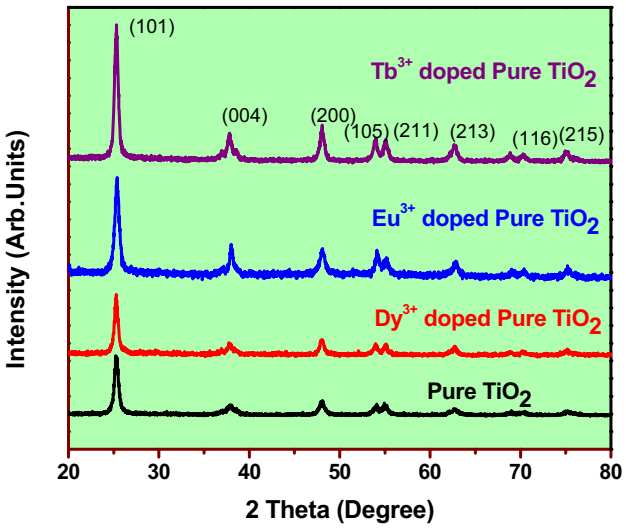

Fig. 2 XRD pattern of pure and Dy^{3+}, Eu^{3+} and Tb^{3+}:TiO_2 nano particles

measurements had been executed at room temperature, the emission spectra were recorded with Fluorescence HITACHI-F-2700 Spectrofluorometer, equipped excitation source with a 150 W Xenon lamp.

3 Results and discussion

3.1 Microstructure analysis—XRD

Figure 2 shows the XRD pattern of pure TiO_2 and Dy^{3+}, Eu^{3+} and Tb^{3+} doped TiO_2 nanoparticles annealed at 400 °C for 4 h. The XRD pattern shows corresponding crystalline planes (101), (004), (200), (105), (211), (213), (116) and (215) of anatase phase with tetragonal structure and matches well with the standard JCPDS 21-1272 [22]. The XRD pattern obtained for all the samples for 0.5 mol% are identical. This indicated that Dy^{3+} Eu^{3+} and Tb^{3+} doping did not have much of an impact on the crystal structure and supported the fact that the ions occupied the cationic sites of the TiO_2 matrix. Furthermore, as per the obtained XRD patterns the intensities corresponding to the samples, Tb^{3+} is high compare to other samples. However, predominate phase in pure and doped TiO_2 is anatase phase and this may be due to the low concentration and dispersion of Dy^{3+}, Eu^{3+} and Tb^{3+} completely in the titania matrix. The diffraction peaks is used to calculate the average crystallite size by using the Debye–Scherrer's principle Eq. (1) [23] for pure, Dy^{3+} ,Eu^{3+} and Tb^{3+} doped TiO_2 are 44.36, 40.36, 33.72 and 34.66 respectively and are shown in Table 1. From the result of Table 1 the average crystallite size was seen to be slightly decreases with changing the dopant, these decrease in the average crystallite size can be ascribed to the fact that RE doping slows the growth of TiO_2 [24].

Further, crystallite size and micro-strain are estimated from the Williamson-Hall plots (W-H plots) based on Eq. (2) [25] by plotting a graph with respect to (w.r.t) 4sinθ (X-axis) and βcosθ (Y-axis), the W-H plots are shown in the Fig. 3. The calculated crystallite sizes were well matched to those estimated using Scherrer's relation but a small increase in the crystallite size can be due to the concern of strain aspect in W-H method. It is also noted that the micro strain is different for pure and Dy^{3+}, Eu^{3+} and Tb^{3+} doped TiO_2.

$$d = \frac{k\lambda}{\beta\ Cos\ \theta} \tag{1}$$

$$\beta Cos\theta = \frac{0.89\ \lambda}{D} + 4\varepsilon\ Sin\theta \tag{2}$$

Table 1 The peak positions, FWHM of diffraction peaks for pure and RE ion doped—TiO_2 nanocrystals

Samples	Peak position (°) 2θ			FWHM (101)	Lattice constant		Grain size (nm)	Strain
	(101)	(004)	(200)		a = b/Å	C/Å		
Pure TiO_2	25.28	37.95	48.08	0.00987	3.785	9.515	44.36	2.53×10^{-3}
0.5 mol% Dy^{3+}:TiO_2	25.22	37.82	48.02	0.01291	3.788	9.495	40.36	3.31×10^{-3}
0.5 mol% Eu^{3+}:TiO_2	25.23	37.80	48.02	0.00889	3.785	9.515	33.72	2.28×10^{-3}
0.5 mol% Tb^{3+}:TiO_2	25.22	37.83	48.01	0.01266	3.786	9.516	34.66	3.24×10^{-3}

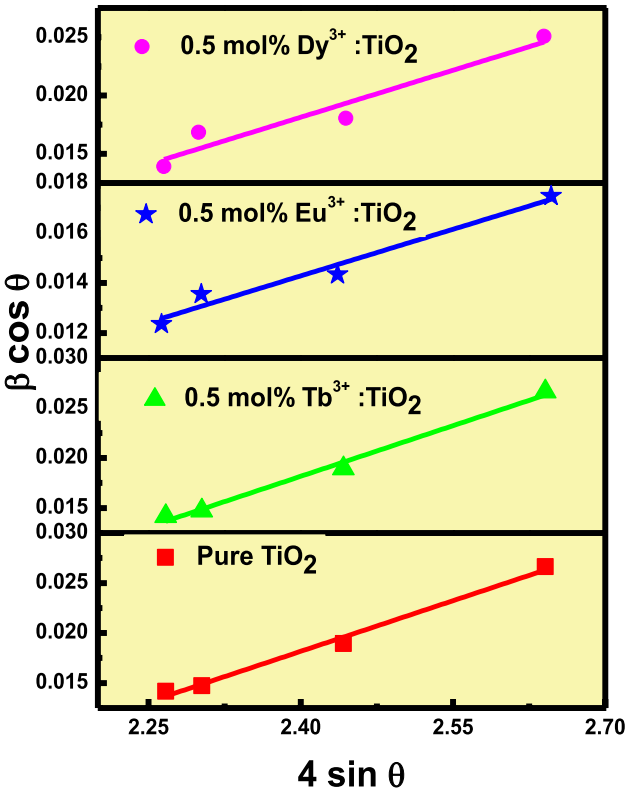

Fig. 3 W-H plots of pure and Dy^{3+}, Eu^{3+} and Tb^{3+}:TiO_2 nano particles

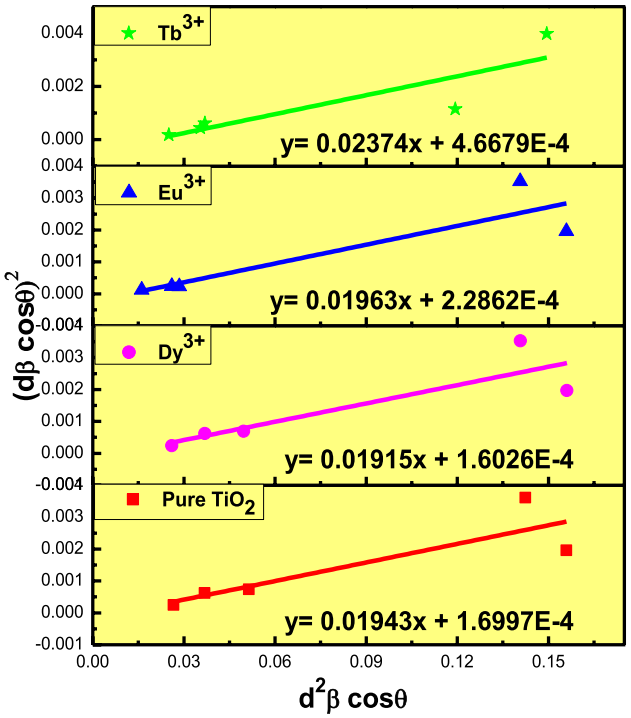

Fig. 4 Size–strain plot of pure and Dy^3, Eu^{3+} and Tb^3:TiO_2 nanoparticles

where 'β' is observed Full Width Half Maxima (FWHM), 'θ' is the Bragg's angle, 'k' is the Scherer's constant, 'λ' is the wavelength X-ray used, 'D' is the crystallite size and 'ε' is the strain present in the crystal. Stain (ε) = β/(4cosθ), as per the equation strain increases w.r.t. the increase in FWHM and the same is reflected in Table 1.

Size–strain plots technique is generally measured for the isotropic nature of the crystal structure. It is expected that the crystallite size profile is called by a Lorentzian function and the size–strain profile by a Gaussian function [26].

$$\left(d_{hkl}\beta_{hkl}\cos\theta\right)^2 = \frac{K}{D}d_{hkl}^2\beta_{hkl}\cos\theta + \left(\frac{\varepsilon}{2}\right)^2$$

where K is a constant that depends on the shape of the particles for spherical shape particles it is given as ¾. The term $\left(d_{hkl}\beta_{hkl}\cos\theta\right)^2$ is plotted with respect to $d_{hkl}^2\beta_{hkl}\cos\theta$. For all orientation peaks of RE doped TiO_2 with the anatase tetragonal phase from 2θ = 15°–80°. The plots are presented in Fig. 4. The strain of the crystallite size is obtained from the slope of the y-axis intercept. The error in the W-H plot to calculate the strain and particle size is found to be 0.01.

From literature it is found that, when the concentration of RE increases from 0.1 mol% to 1 mol%, the periodic crystal lattice of TiO_2 get strained and the maximum solubility limits for Eu^{3+}, Tb^{3+} and Dy^{3+} and is found to be 0.5 mol%. Further increase in the concentration of dopant above the solubility limit it shows a decrease in both the strain and the lattice constant [27, 28]. This may be due to the arrangement of Dy^{3+}, Eu^{3+} and Tb^{3+} on the crystallite surface or interstitials of TiO_2 nanocrystals. It is evident from the graph that the position of (101) is at 25.28° for undoped TiO_2. But for the doped samples i.e. TiO_2:Dy^{3+}, TiO_2:Eu^{3+} and TiO_2:Tb^{3+} the position of peak (101) shifts towards the origin or towards the lower diffraction angles. It is also observed that the positions are almost invariant and is around 25.22° for all RE doped TiO_2. This indicates that the incorporation of the RE dopants is responsible for shifting in peak positions [29]. The amalgamation of RE in TiO_2 lattice results in deformation of the lattice arrangement by dislocating Ti^{4+} ion due to mismatch in the ionic radii between RE and Ti^{4+} [30]. The powders formed showed tensile strain that may be due to the grain growth and densification. Lattice constants varied with incorporation of different RE and are shown in Table 1. Unit cell volume and lattice constant 'c' of anatase phase increased with the change of RE dopant where lattice constant 'a' remain approximately constant. This may be due to the increase in crystallite size and crystallinity of the TiO_2 anatase phase.

3.2 Morphology analysis—FESEM

Figure 5a–c shows the FESEM images and EDS spectrum of pure and Dy^{3+}, Eu^{3+} and Tb^{3+} doped TiO_2 nanoparticles shows the structural morphology. The majorities of TiO_2 particles are spheroid or oblate spheroid and look looser, and some macro pores could be seen on some nanoparticles. The FESEM images show for all samples consistent distribution of particles, which consist of cluster particle or single particle. Pure and Dy^{3+}, Eu^{3+} and Tb^{3+} doped TiO_2 shows a narrow size distribution of 45 nm, 40 nm, 35 nm and 35 nm (approximately) respectively. By 0.5 mol% the doping concentration of Dy^{3+}, Eu^{3+} and Tb^{3+} into titania matrix, the average size of the titania nanoparticles decreases exponentially from 45 to 35 nm, respectively. The presence of particles and the distribution of elements are investigated by the EDS element analysis Fig. 5a–c shows the result of the EDS analysis of TiO_2: (Dy^3: Eu^{3+}: Tb^3) nanoparticles the presence of Ti, O, Dy, Tb and Eu with other impurities, the analysis of EDS spectrum concludes that the surface contains Ti, O, Dy, Tb and Eu, which confirms the formation of RE^{3+} doped TiO_2 nanoparticles. This shows that the

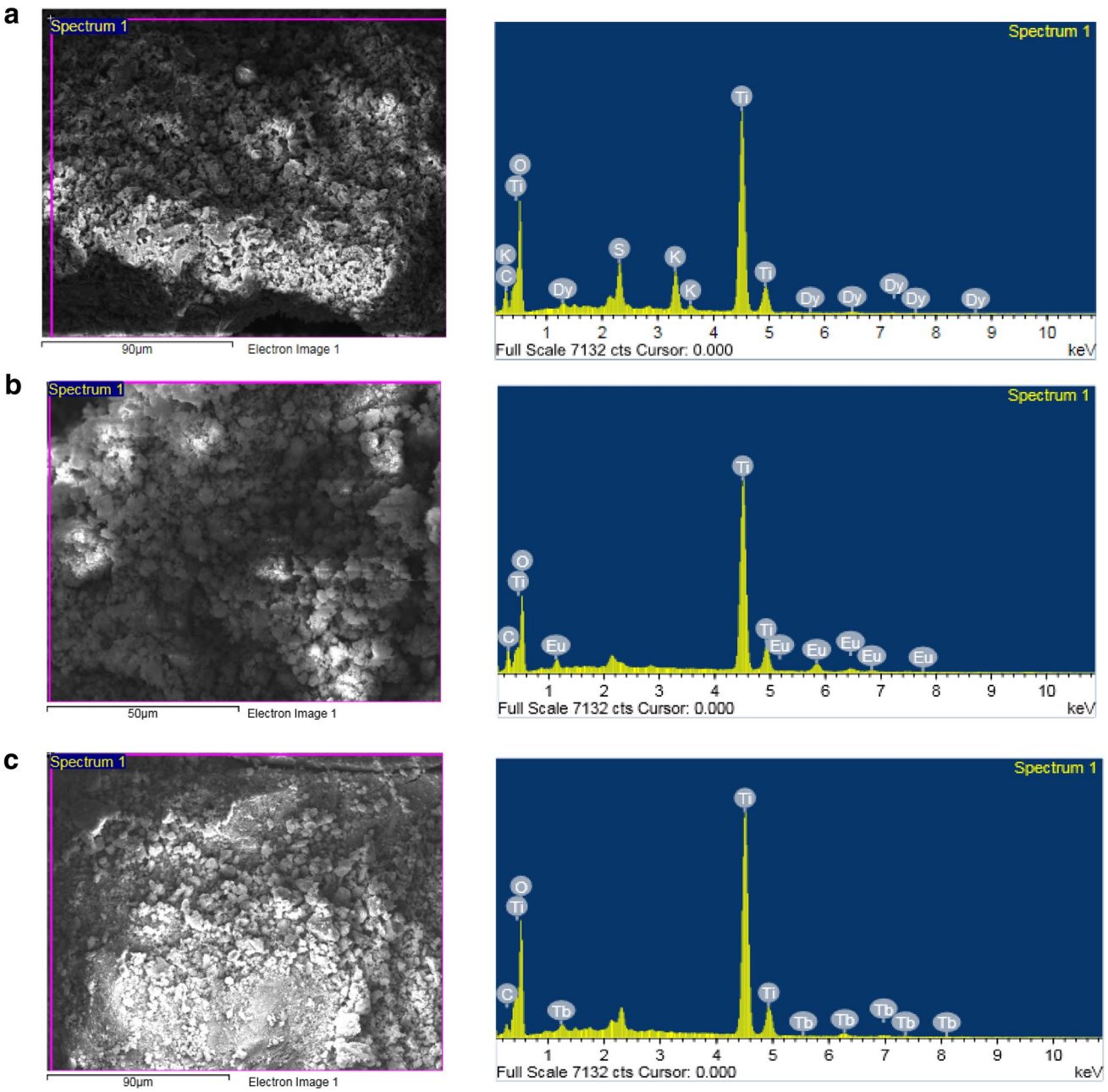

Fig. 5 FESEM images and EDS spectrum of **a** TiO_2: Dy^{3+} **b** TiO_2: Eu^{3+} and **c** TiO_2: Tb^{3+} nanoparticles

materials made were of non-stoichiometric with oxygen vacancy that indicates the enhanced photocatalytic activity [29]. This may be due to the incorporation of Dy^{3+}, Eu^{3+} and Tb^{3+} ions which suppresses the growth of TiO_2 nanocrystals to a greater extent. It is similar to the values calculated from XRD analysis.

3.3 Morphology analysis by TEM

The TEM image of the RE^{3+}:TiO_2 nanoparticles was shown in Fig. 6a–d. High resolution lattice fringe image confirmed that the sample as comprise of associated crystalline titania nanoparticles leaning generally in one direction, corresponding to (101) interplaner spacing ($d_{101} = 0.352$ nm, $d_{004} = 0.243$) of anatase TiO_2 phase strongest intensity in selected area electron diffraction (SAED). The SAED images taken from these nanocrystalline particles are in Fig. 6a–d. The result evidently revealed the unique occurrence of (101) and (004) concentric diffraction rings with d-spacing approximately being 0.35 nm and 0.24 nm indicating the excellent crystalline nature of RE^{3+}. Many spherical shaped RE doped TiO_2 nanoparticles dispersed homogeneously in the TiO_2 matrix with wide size distribution ranging from 18 to 41 nm have been observed from TEM micrographs. The average crystallite size calculated for TiO_2 from Scherrer formula, W-H plots and size–strain plots using XRD data were matched relatively well with the crystallite size measured form TEM micrograph.

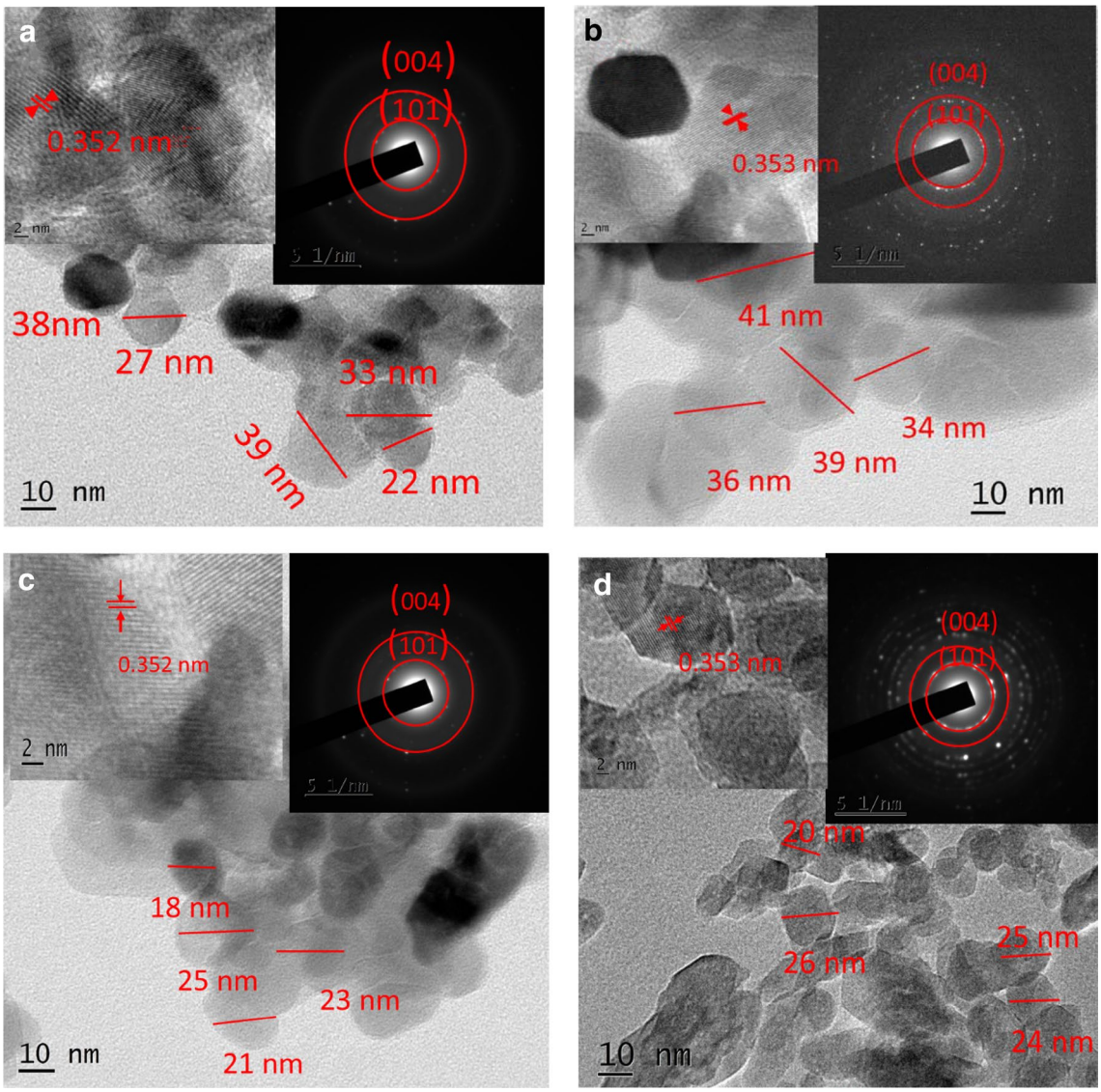

Fig. 6 TEM images of **a** Pure TiO_2 **b** TiO_2: Dy^{3+} **c** TiO_2: Eu^{3+} and **d** TiO_2: Tb^{3+} nanoparticles

3.4 Optical analysis by UV–visible spectroscopy

In order to determine the nature of the optical band gap as either direct or indirect, consider the variation of the absorption co-efficient with energy [31]. Figure 7 shows absorption spectra of the Dy^{3+}, Eu^{3+} and Tb^{3+} doped TiO_2 nanoparticles clear observations determines that the absorption spectrum slightly shifted to blue region and is attributed to the quantum size impact. These confirmed that Dy^{3+}, Eu^{3+} and Tb^{3+} dopant did not give to new spectrum phenomena and will inhabit the increases of anatase crystallite. Kubelka–Munk function [15] was applied with the purpose to transform the diffuse reflectance to absorption co-efficient (α) from Eq. (3).

$$\alpha \approx \frac{K}{S} = \left[\frac{\left(1-R_\infty\right)^2}{2R_\infty}\right] = F\left(R_\infty\right) \tag{3}$$

where K and S are absorption and scattering co-efficient, the reflectance R_∞ is

$$R_\infty = \frac{R_{(measured)}}{R_{(standard)}}$$

The use of the Tauc relation $(\alpha h\vartheta)^\gamma = a\left(h\vartheta - E_g\right)$, the value of direct band gap E_g of all the sample had been calculated. In this relation 'α' is absorption co-efficient, 'h' is Planck constant, 'ϑ' is frequency of the light and E_g is the energy band gap. The power co-efficient 'ϑ' is characteristics of the sort of transition and $\vartheta = 1/2$ for direct or $\vartheta = 2$ for indirect allowed transitions of the semiconductors [7, 32, 33].

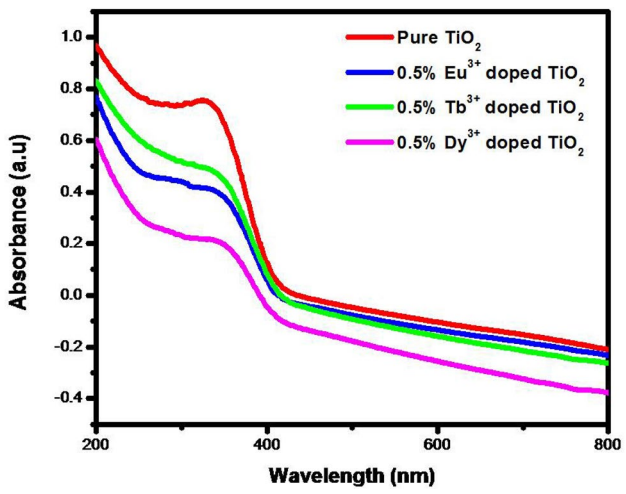

Fig. 7 UV–VIS absorption spectrum of pure and Dy^3, Eu^{3+} and Tb^3:TiO_2 nanoparticles

In Fig. 8 shows the $(\alpha h\vartheta)^2$versus E (eV) plots for the direct band gap transition for pure and 0.5 mol% concentration Dy^{3+}, Eu^{3+} and Tb^{3+} doped TiO_2, where E_g (bandgap) is obtained through extrapolating the linear part of the curve to meet the x-axis. Table 2 shows direct band gap of synthesized pure, Dy^{3+}, Eu^{3+} and Tb^{3+} doped TiO_2 for 0.5 mol% are found to be 3.20, 3.16, 3.14 and 3.17 eV respectively. The difference in the value of band gap obtained may be due to incorporation of different RE ions and those are attributed to the $X_1 \rightarrow X_1$ transition [34]. The results demonstrate that the Dy^{3+}, Eu^{3+} and Tb^{3+} doping results decrease the band gap of anatase TiO_2.

3.5 Photoluminescence analysis

Photoluminescence spectroscopy is a tool to records about the photoelectric and electro-optic characteristics of nanomaterial, Figs. (9–11) illustrates the emission spectra for RE doped (Dy^{3+}:Eu^{3+}:Tb^{3+}):TiO_2, with 0.5 mol% concentration with excitation wavelengths of 345 nm, 376 nm and 350 nm respectively, it is very exciting to observe that most emission intensity within the visible region relies upon dopant concentration. Pure TiO_2 nanoparticles does not show any emission peak, when it get excited by a light of wavelength 355–386 nm. This may be due to non-irradiative transition via lattice phonons and/or surface states. However, at the 0.5 mol% concentration of dopant (Dy^{3+}:Eu^{3+}:Tb^{3+}):TiO_2, nanoparticles show three distinct emission peaks for each dopant. For Eu^{3+} in Fig. 9, shows 590 nm, 620 nm and 650 nm emission bands and corresponding transitions are $^5D_0 \rightarrow {}^7F_1$, $^5D_0 \rightarrow {}^7F_2$ and $^5D_0 \rightarrow {}^7F_3$ [35, 36]. Generally, there are two possibilities of Eu^{3+} incorporation in TiO_2 nanocrystals: substitutional or interstitial. Both cases produce localized levels inside the gap thus contributing to the characteristic PL response. The Eu^{3+} doped phosphor nanoparticles show sharp and well-resolved emission lines associated with Eu^{3+} ions which correspond to radiative relaxations from the $^5D_0$ level to its low-lying multiplets ^7F_J. The strongest emission centred at around 620 nm corresponds to the electrical dipole transition $^5D_0 \rightarrow {}^7F_2$ of Eu^{3+} ions which give the red color in the luminescence signals. In the literature, it has been reported that this transition is possible only if Eu^{3+} ions occupy a site without an inverse symmetry. In Fig. 10, it was remarkable that $^5D_3 \rightarrow {}^7F_6$ transition was responsible for the blue emission lower 480 nm, while the green emission beyond 480 nm results from the $^5D_4 \rightarrow {}^7F_5$ transition. Various Tb^{3+} activated materials display a blue emission from the $^5D_3$ level and a green emission from the $^5D_4$ level. In the present work, the emission bands for Tb^{3+} at 480 nm, 545 nm, 585 nm and 620 nm corresponding transitions are $^5D_4 \rightarrow {}^7F_6$, $^5D_4 \rightarrow {}^7F_5$, $^5D_4 \rightarrow {}^7F_4$ and $^5D_4 \rightarrow {}^7F_3$ [37–39]. Visible luminescence of Tb^{3+} was predominantly

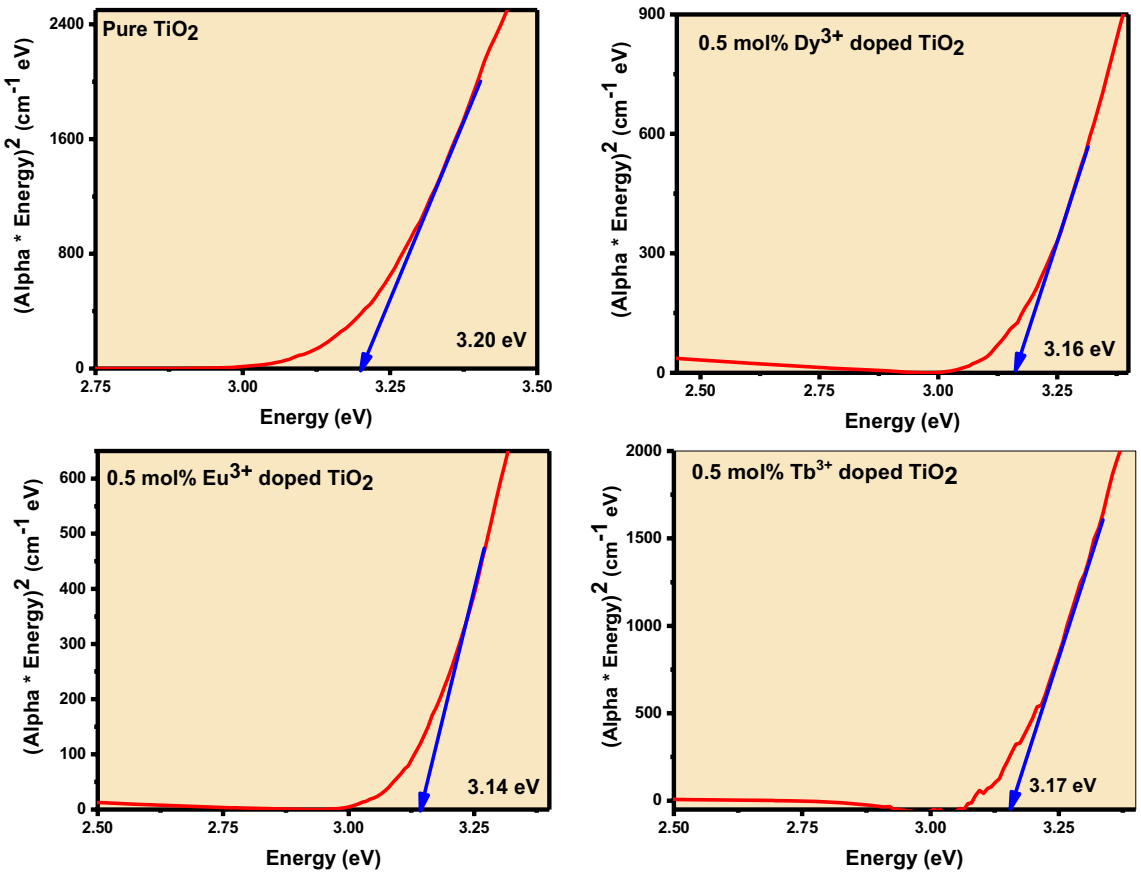

Fig. 8 Kubelka–Munk plots and band gap energy estimation of sample for direct transition

Table 2 Optical band gap of pure and RE ion doped TiO_2

Samples	Optical band gap (eV)
Pure TiO_2	3.20
Dy^{3+}: TiO_2	3.16
Eu^{3+}: TiO_2	3.14
Tb^{3+}: TiO_2	3.17

because of the transitions from $^5D_3$ and $^5D_4$ to ^7F_J. It has been proven that the spectral distribution was significantly dependent on the amount of terbium, when the concentration of Tb^{3+} was low, emissions from both of the excited states are observed in most Tb^{3+} activated phosphors. In the case of Dy^{3+} :TiO_2 Fig. 11 have also three emission bands at 378 nm, 470 nm and 565 nm [40]. It was found that when the (Dy^{3+}:Eu^{3+}:Tb^{3+}):TiO_2, at 0.5 mol% concentration, the periodic crystal lattice of TiO_2 gets strained. Therefore Dy^{3+}:Eu^{3+}: Tb^{3+} might have preference for substituting the Ti ions in the lattice and eventually generates number of oxygen vacant sites in host TiO_2 nanoparticles [41]. These oxygen vacancies might be useful to enhance the

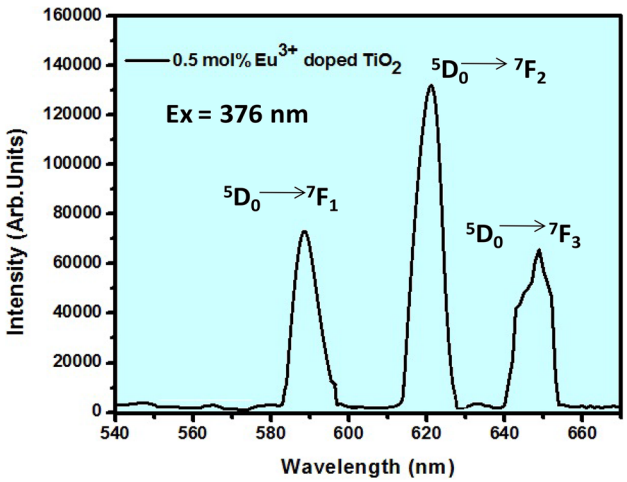

Fig. 9 Emission spectra of Eu^{3+}doped TiO_2 obtained at excitation 376 nm

emission behavior of rare-earth ions by acting as sensitizers for efficient energy transfer from charge transfer state to Dy^{3+}, Eu^{3+} and Tb^{3+} ions [42]. Moreover above 0.5 mol% of Dy^{3+}, Eu^{3+} and Tb^{3+} emissions were completely due to

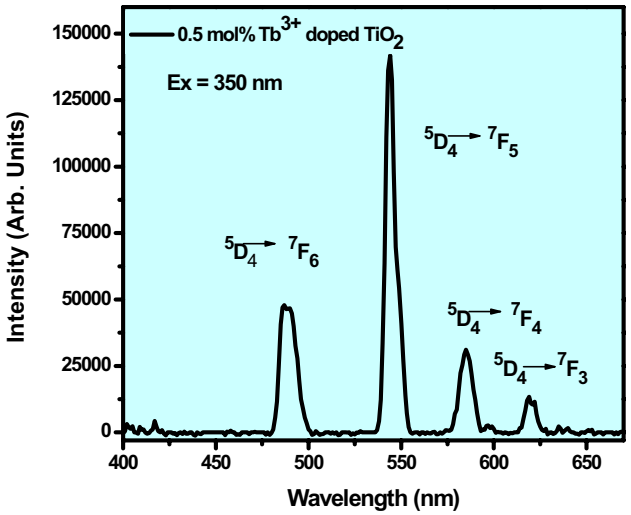

Fig. 10 Emission spectra of Tb^{3+}doped TiO_2 obtained at excitation 350 nm

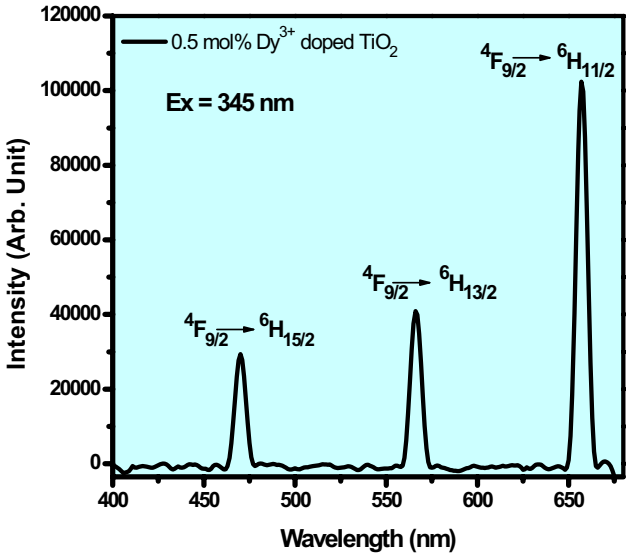

Fig. 11 Emission spectra of Dy^{3+}doped TiO_2 obtained at excitation 345 nm

oxygen vacancies. These luminescence properties were similar with those previously investigated [43]. The energy level diagram for Dy^{3+}, Eu^{3+} and Tb^{3+} doped TiO_2 is shown in the Fig. 12. In this article the Dy^{3+} ions are excited by 345 nm (28,982 cm^{-1}) as a result the ions are excited to $^6P_{7/2}$ and from there the ions are de-excited to $^4F_{9/2}$ by a phenomenon of non-radiative transitions. Thus from $^4F_{9/2}$ level respective transition takes place with characteristics emissions and is shown in the figure. A similar transition occurs in case of Eu^{3+} and Tb^{3+} doped TiO_2. The PL spectrum of Dy^{3+}, are associated to the visible region the transitions $^4F_{9/2} \rightarrow {}^6H_{15/2}$ for the emission 470 nm $^4F_{9/2} \rightarrow {}^6H_{13/2}$ for emission 565 nm and $^4F_{9/2} \rightarrow {}^6H_{11/2}$ for emission 657 nm respectively. Therefore from this research work we bring to a close that, the enhancement of luminescence even at lesser concentration of Dy^{3+}dopant can be better to the satisfactory feasible data with decrease excitation energy [44].

3.6 Color chromaticity coordinate

As to shading, the human visualization reacts to trichromatic lifts on the virtual cortex, assessed by the Commission Internationale de L'Eclairage (CIE) [45, 46] in three coordinating limits powerful spectral bands, A (λ), B (λ) additionally C (λ), open as free-get to tables. Chromaticity outline is a graphical portrayal of tristimulus values, which describe conceivable colors, shaped by a triangle with vertices controlled by colors value [47]. The 'A' and 'B' CI facilitates for the fluorescence emission of TiO_2 in different REs were figured by Eqs. (4) and (5) from their x, y and z tristimulus integrations of Eq. (6–8). Using photoluminescence results it is conceivable to make a graph of integrated PL intensity for each dopant as appeared in Fig. 13.

$$A = x/(x + y + z) \tag{4}$$

$$B = y/(x + y + z) \tag{5}$$

$$x = \int_{250}^{750} I(\lambda)\bar{A}(\lambda)d\lambda \tag{6}$$

$$x = \int_{250}^{750} I(\lambda)\bar{B}(\lambda)d\lambda \tag{7}$$

$$x = \int_{250}^{750} I(\lambda)\bar{C}(\lambda)d\lambda \tag{8}$$

The chromaticity diagram Fig. 11 of (Dy^{3+}:Eu^{3+}:Tb^{3+}):TiO_2 (0.5 mol%) under the excitation wavelength of 355–386 nm, it is very clear that color coordinates indicated as a different symbol and those are lies in different color region. Thus, with respective of the concentration of the different RE ions, the color coordinates change accordingly. For Eu^{3+}:TiO_2 which falls in Red color with CIE coordinates of range x = 0.62 and y = 0.34. Green region of CIE graph corresponding to x = 0.35 and y = 0.48 values for Tb^{3+} doped TiO_2. The growth in PL intensity for all doped sample is because of the self trapped excitations recombination which is a blended effect of defect centers generated from oxygen vacancies and particle size. Dy^{3+} doped TiO_2 at 345 nm excitation a CIE chromaticity coordinates value x = 0.32 and y = 0.35 generates clear white color. The color difference observed in the CIE graph probably is due to photophysical characteristics of different dopant environment with mol% concentration of material network structure. This result clearly indicates that by doping Dy^{3+} ions can be an effective process for the development of high

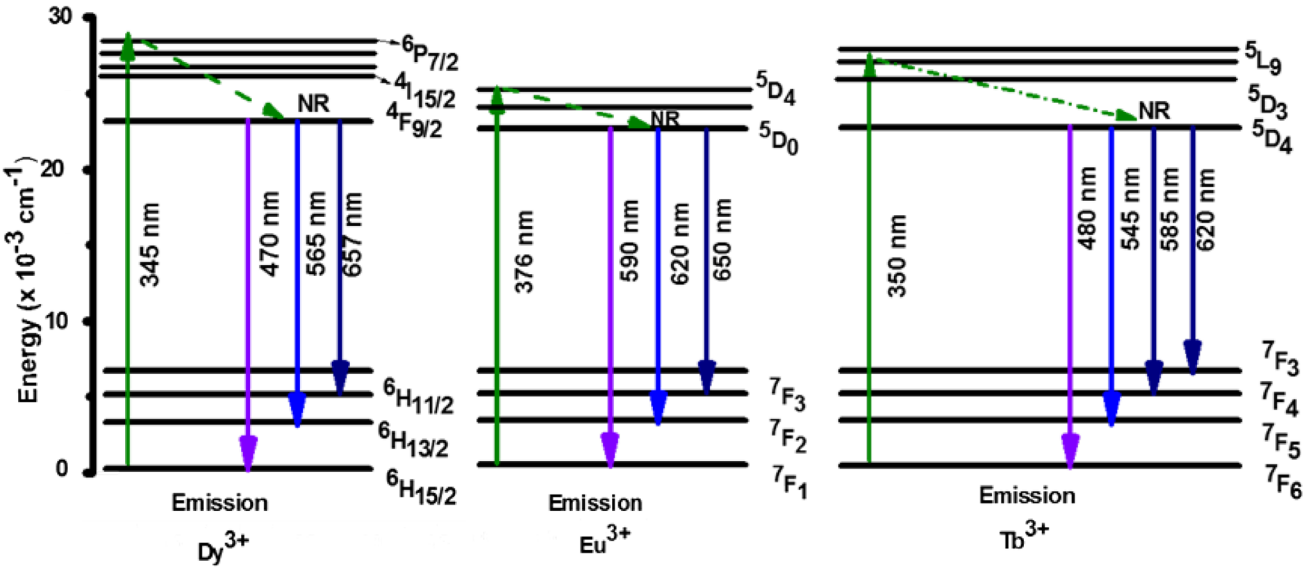

Fig. 12 Energy level diagram of Dy^{3+}, Eu^{3+} and Tb^{3+} ion

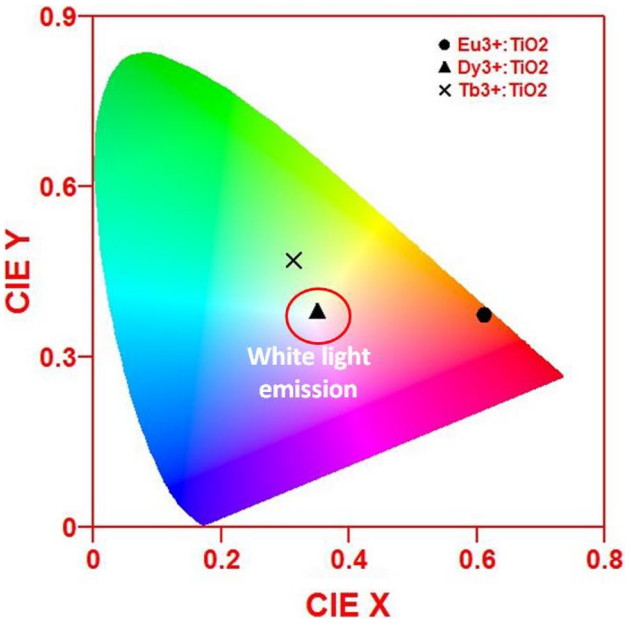

Fig. 13 CIE chromaticity diagram of Dy^{3+}, Eu^{3+} and Tb^{3+}: TiO_2 (0.5 mol%) nanophosphor

efficiency white light emitting diodes. These consequences are propelling for a significant comprehension of emission modification approaches and the new material engineering along with desirable scenery.

Table 3 Represent the CIE color coordinates with color purity of different RE

Sample	X	Y	% of color purity
Dy^{3+}: TiO_2	0.32	0.35	91
Eu^{3+}: TiO_2	0.62	0.34	84
Tb^{3+}: TiO_2	0.35	0.48	73

3.7 Color purity

The color purity is a numerically based color co-ordinate system used to authentify the nature of the hue of the nanophosphor and is calculated by following Eq. 9.

$$Color\ purity = \frac{\sqrt{(x - x_{ee})^2 + (y - y_{ee})^2}}{\sqrt{(x_d - x_{ee})^2 + (y_d - y_{ee})^2}} \times 100 \quad (9)$$

where (x, y) are the co-ordinates corresponding to sample point, (x_{ee}, y_{ee}) are the co-ordinated of illumination points and (x_d, y_d) are the dominant wavelengths. The variation of color co-ordinates is shown in the Table 3. It is evident from the above table that the color co-ordinates corresponding to 0.5 mol% concentration of Dy^{3+}, Eu^{3+} and Tb^{3+} is closure to ideal white light (0.33, 0.33), red light (0.67, 0.33) and green light (0.31, 0.59) the color purity is found to be 91%, 84% and 73% for the excitation of 345 nm, 376 nm and 350 nm respectively. This result clearly suggests that by doping Dy^{3+} ions can be an effective process for the development of high

efficient white light emitting diodes. Furthermore, the nanophosphors can be a potential candidate in the field of solid state lightning. Eu^{3+} doping TiO_2, a red color with high light emitting resistor (LER) value and luminous flux is useful as a red light source for LED and display device applications. Emitted light can be characterized by dominant wavelength and color purity. The desirable CIE chromaticity co-ordinates (0.35, 0.48) and high color purity (76%) of Tb^{3+}: TiO_2 nanophosphors The calculated chromaticity co-ordinates for Tb^{3+}: TiO_2 nanophosphors are near the standard chromaticity co-ordinates for excellent green phosphors and thus are promising green producers for WLED applications [48].

4 Conclusion

Pure TiO_2 and (Dy^{3+}:Eu^{3+}:Tb^{3+}):TiO_2 nanoparticles have been prepared successfully using hydrothermal method. The XRD analysis confirmed that predominately the pure TiO_2 and (Dy^{3+}:Eu^{3+}:Tb^{3+}):TiO_2 nanoparticles show anatase phase. The average sizes of the nanoparticles are in the range of 45–35 nm. Absorption studies reveal band gap broadening for RE-doped TiO_2 nanophosphors. PL spectra exposed that the intensity of the blue emission corresponding $^4F_{9/2} \rightarrow {}^6H_{15/2}$ and yellow emission corresponding $^4F_{9/2} \rightarrow {}^6H_{13/2}$ is frequently noticeable than the blue band in its emission spectrum showing that Dy^{3+} will radiate white light. The color purity of the studied samples is found to be 91% for Dy^{3+}, 84% for Eu^{3+} and 73% for Tb^{3+} at the excitation of 345 nm, 376 nm and 350 nm respectively. At lower concentration of RE doping an enhanced luminescence is observed for TiO_2 based hybrid semiconductors for optoelectronic applications.

Acknowledgements The authors are grateful to the DST (SERB) New Delhi for providing financial support through major project No. SR/S2/CMP/-0069/2012. Thanks to Prof. Sharath Ananthamurthy, Coordinator DST-PURSE Programme for XRD characterization Bangalore University, Bengaluru and thanks Directorate of Minorities, Government of Karnataka.

References

1. B.O. Regan, M. Gratzel, Nature **353**, 737 (1991)
2. J. Zhang, J. Lin, J. Wu, S. Zhang, P. Zhou, X. Chen, R. Xu, J. Mater. Sci. Mater. Electron. **27**, 1350 (2016)
3. P. Sanjay, K. Deepa, J. Madhavan, S. Senthil, Mater. Lett. **219**, 158 (2018)
4. K.M. Butt, M.A. Farrukh, I. Muneer, J. Mater. Sci. **27**, 8493 (2016)
5. Y. Ghayeb, M.M. Momeni, A. Mozafari, J. Mater. Sci. Mater. Electron. **27**, 11804 (2016)
6. S. Rehman, R. Ullah, A.M. Butt, N.D. Gohar, J. Hazard. Mater. **170**, 560 (2009)
7. M.M. Momeni, Y. Ghayeb, J. Solid State Electrochem. **20**, 683 (2016)
8. M. Khairy, W. Zakaria, Egypt. J. Pet. **23**, 419 (2014)
9. B. Singh, G. Kaur, P. Singh, K. Singh, J. Sharma, M. Kumar, R. Bala, R. Meena, S.K. Sharama, A. Kumar, New J. Chem. **41**, 11640 (2017)
10. R. Dhabbe, A. Kadam, P. Korake, M. Kokate, P. Waghmare, K. Garadkar, J. Mater. Sci. **26**, 554 (2015)
11. B. Roose, S. Pathak, U. Steiner, Chem. Soc. Rev. **44**, 8326 (2015)
12. J.J. Wu, C.C. Yu, J. Phys. Chem. B **108**, 3377 (2004)
13. Y. Li, M. Guo, M. Zhang, X. Wang, Mater. Res. Bull. **44**, 1232 (2009)
14. K.V. Arun Kumar, K.P. Revathy, P. Vasudevan, S. Thomas, P.R. Biju, N.V. Unnikrishnan, J. Rare Earths **31**, 441 (2013)
15. S. Ezhil Arasi, M. Victor Antony Raj, J. Madhavan, J. Mater. Sci. Mater. Electron. **29**, 3170 (2018)
16. C. Jayachandraiah, K.S. Kumar, G. Krishnaiah, N.M. Rao, J. Alloys Compd. **248**, 623 (2015)
17. Y. Cao, Z. Zhao, J. Yi, C. Ma, D. Zhou, R. Wang, C. Li, J. Qiu, J. Alloys Compd. **12**, 554 (2013)
18. M. Dalvandi, B. Ghasemi, J. Sol-Gel Sci. Technol. **68**, 66 (2013)
19. S.A. Pawar, R.S. Devan, D.S. Patil, V.V. Burungale, T.S. Bhat, S.S. Mali, S.W. Shin, J.E. Ae, C.K. Hong, Y.R. Ma, J.H. Kim, P.S. Patil, Electrochim. Acta **117**, 470 (2014)
20. J. Yin, L. Xiang, X. Zhao, Appl. Phys. Lett. **90**, 113112 (2007)
21. V. Ahmed Yasir, P.N. Mohan Das, K.K.M. Yusuff, Int. J. Inorg. Mater. **3**, 593 (2001)
22. Ž. Antić, R.M. Krsmanović, M.G. Nikolić, M. Marinović-Cincović, M. Mitrić, S. Polizzi, M.D. Dramićanin, Mater. Chem. Phys. 135, 1064 (2012)
23. A.S. Nasab, M. Maddahfar, S. Mostafa, J. Mol. Liq. **216**, 1 (2016)
24. K. Naeem, F. Ouyang, Phys. B **405**, 221 (2010)
25. A. Taherniya, D. Raoufi, Semicond. Sci. Technol. **31**, 125012 (2016)
26. S. Anand, A. Persis Amaliya, M. Asisi Janifer, S. Pauline, Mod. Electron. Mater. **3**, 168 (2017)
27. D. Wojcieszak, D. Kaczmarek, J. Domaradzki, E. Prociow, A. Morawski, M. Janus, Cent. Eur. J. Phys. **9**, 354 (2011)
28. Y. Cheng, M. Zhang, G. Yao, L. Yang, J. Tao, Z. Gong, G. He, J. Alloys Compd. **179**, 662 (2016)
29. J.G. Dos Santos, T. Ogasawara, R.A. Correa, Braz. J. Chem. Eng. **03**, 555 (2009)
30. M.S. Suwarnkar, G.V. Khade, S.B. Babar, K.M. Garadkar, J. Mater. Sci. Mater. Electron. **28**, 17140 (2017)
31. A.L. Yerokhin, X. Nie, A. Leyland, A. Matthews, S.J. Dowey, Surf. Coat. Technol. **122**, 73 (1999)
32. R. Mechiakh, N. Bensedrine, R. Chtourou, Appl. Surf. Sci. **257**, 9103 (2011)
33. S.E. Arasi, J. Madhavan, M.V. Antony Raj, J. Taibah Univ. Sci. **12**, 186 (2018)
34. N. Daude, C. Gout, C. Jouanin, Phys. Rev. B **15**, 3229 (1977)
35. A. Chakraborty, G.H. Debnath, N.R. Saha, D. Chattopadhyay, D.H. Waldeck, P. Mukherjee, J. Phys. Chem. C **120**, 23870 (2016)
36. S. Stojadinovic, N. Radic, B. Grbic, S. Maletic, P. Stefanov, A. Pacevski, R. Vasilic, Appl. Surf. Sci. **370**, 218 (2016)
37. A.J. Peter, I.B.S. Banu, J. Mater. Sci. **25**, 2771 (2014)
38. M. Ye, L. Zhou, F. Hong, L. Li, Q. Xia, K. Yang, X. Xiong, Opt. Mater. **47**, 161 (2015)
39. K.P. Mani, G. Vimal, P.R. Biju, C. Joseph, N.V. Unnikrishnan, M.A. Ittyachen, Spectrochim. Acta A **148**, 412 (2015)
40. D. Kim, D. Park, N. Oh, J. Kim, E.D. Jeong, S.J. Kim, S. Kim, J.C. Park, Inorg. Chem. **54**, 325 (2015)
41. C.R. Shyniya, K. Amarsingh Bhabu, T.R. Rajasekaran, J. Mater. Sci. Mater. Electron. **28**, 6959 (2017)
42. Q.G. Zeng, Z.M. Zhang, Z.J. Ding, Y. Wang, Y.Q. Sheng, Scr. Mater. **57**, 897 (2007)
43. H. Deng, N. Xue, Z. Hei, M. He, T. Wang, N. Xie, R. Yu, Opt. Mater. Express **5**, 490 (2015)

44. G.S. Rama, J. Young, H. Chae, B. Kee, J. Hyun, J. Hwan, Curr. Appl. Phys. **9**, 92 (2009)
45. V.H. Rao, P.S. Prasad, M. Mohan Babu, P.Venkateswara Rao, T. Satyanarayana, F. Luís, Santos, N. Veeraiah, Spectrochim. Acta A **188**, 516 (2018)
46. M. Kumar, T.K. Seshagiri, M. Mohapatra, V. Natarajan, S.V. Godbole, J. Lumin. **132**, 2810 (2012)
47. K. Thomas, D. Alexander, S. Sisira, P.R. Biju, N.V. Unnikrishnan, M.A. Ittyachen, C. Joseph, J. Mater. Sci. Mater. Electron. **28**, 17702 (2017)
48. V. Kumar, P. Rani, D. Singh, S. Chawla, RSC Adv. **4**, 36101 (2014)